ARTICLES
PUBLISHED ONLINE: 6 JUNE 2016 | DOI: 10.1038/NPHYS3782
nature physics

# Topological semimetals with helicoid surface states

Chen Fang[1,2*†], Ling Lu[1,2†], Junwei Liu[1] and Liang Fu[1*]

**We show that the surface dispersions of topological semimetals map to helicoidal structures, where the bulk nodal points project to the branch points of the helicoids whose equal-energy contours are Fermi arcs. This mapping is demonstrated in the recently discovered Weyl semimetals and leads us to predict new types of topological semimetals, whose surface states are represented by double- and quad-helicoid surfaces. Each helicoid or multi-helicoid is shown to be the non-compact Riemann surface representing a multi-valued holomorphic function (generating function). The intersection of multiple helicoids, or the branch cut of the generating function, appears on high-symmetry lines in the surface Brillouin zone, where surface states are guaranteed to be doubly degenerate by a glide reflection symmetry. We predict the heterostructure superlattice $[(SrIrO_3)_2(CaIrO_3)_2]$ to be a topological semimetal with double-helicoid surface states.**

The study of topological semimetals[1,2] has seen rapid progress since the theoretical proposal of a three-dimensional Weyl semimetal in a magnetic phase of pyrochlore iridates[3]. In general, topological semimetals are materials where the conduction and the valence bands cross in the Brillouin zone and the crossing cannot be removed by perturbations preserving certain crystalline symmetry such as the lattice translation. Bloch states in the vicinity of the band crossing possess a non-zero topological index—for example, the Chern number in the case of Weyl semimetals. The nontrivial topology gives rise to anomalous bulk properties of topological semimetals such as the chiral anomaly[4–6]. Several classes of topological semimetals have been theoretically proposed so far, including Weyl[3,7–15], Dirac[16–20] and nodal line semimetals[2,8,20–32], some among which have been experimentally observed[33–49].

Surface states of topological semimetals have attracted much attention. On the surface of a Weyl semimetal, the Fermi surface consists of open arcs connecting the projection of bulk Weyl points onto the surface Brillouin zone[3], instead of closed loops. The presence of Fermi arcs on the surface is a remarkable property that directly reflects the nontrivial topology of the bulk, and plays a key role in the experimental identification of Weyl semimetals[34,35,38]. In contrast, as shown by recent theoretical works[21,24,26,27,30,50,51], existing Dirac and nodal line semimetals do not have robust Fermi arcs that are stable against symmetry-allowed perturbations. Therefore, the general condition for protected Fermi arcs to appear in topological semimetals remains an open question.

In this work, we report the discovery of a new topological semimetal phase in a wide variety of non-symmorphic crystal structures with the glide reflection symmetry, a combination of a reflection and a half-lattice translation. Such non-symmorphic topological semimetals have either Dirac points or Weyl dipoles in the bulk, which are associated with a $Z_2$ topological invariant that we define. These band crossing points are pairwise connected by symmetry-protected Fermi arcs on the surface, with a unique connectivity determined by the $Z_2$ topological charge. These surface states have a energy–momentum dispersion that can be mapped to an intersecting multi-helicoid structure, where the intersections between helicoids are protected from being gapped by non-symmorphic symmetries, and are hence dubbed 'helicoid surface states'. By relating the $Z_2$ topological index to rotation eigenvalues of energy bands, we provide a simple criterion for the non-symmorphic topological semimetal phase and predict its material realization in the recently synthesized superlattice heterostructure of iridates[52] $[(SrIrO_3)_{2m}(CaIrO_3)_{2n}]$. Interestingly, we find that each multi-helicoid structure is the non-compact Riemann surface[53] of a generating function: a multi-valued holomorphic function whose singularities correspond to the projections of the bulk nodes.

## Helicoid surface states of Weyl semimetals: a revisit

We start by considering the energy–momentum relation $E(\mathbf{k}_\parallel)$ of the surface states of Weyl semimetals, where $\mathbf{k}_\parallel$ is the surface momentum. $E(\mathbf{k}_\parallel)$ is bounded by the bulk conduction and valence band edges in the bulk cones (see the head-to-head cones in Fig. 1a), obtained by collapsing energies of bulk states with the same $\mathbf{k}_\parallel$ at different perpendicular momenta $k_z$. In the most generic case, we assume that there be $N_s$ surface bands, $E_1(\mathbf{k}_\parallel) < E_2(\mathbf{k}_\parallel) < \cdots < E_{N_s}(\mathbf{k}_\parallel)$. Consider a loop in the surface Brillouin zone enclosing the projection of the Weyl point. The Chern number of the Weyl point dictates that[3] the surface dispersion along the loop must be chiral, such that as a $\mathbf{k}$-point moves one round along the loop anticlockwise (clockwise), the energy of the state does not return to the same value, but moves one band higher (lower), that is, $E_n(\mathbf{k}_\parallel) \to E_{n+1}(\mathbf{k}_\parallel)$ ($E_n(\mathbf{k}_\parallel) \to E_{n-1}(\mathbf{k}_\parallel)$). As $\mathbf{k}_\parallel$ keeps circling the loop anticlockwise (clockwise), the band index keeps increasing (decreasing) before the state merges into the conduction (valence) bulk. In this process, the dispersion along the loop maps out a spiral[54] that connects the two bulk cones, and as one sweeps the radius of the loop, the spirals at different radii form a helicoid, as shown in Fig. 1a. For any given energy, each spiral crosses the energy an odd number of times, so the iso-energy contour of the helicoid must be an open arc emanating from the centre.

The winding of the energy dispersion along any loop enclosing the Weyl point is the same as the winding of the phase of a holomorphic function along any loop enclosing a simple (linear

[1]Department of Physics, Massachusetts Institute of Technology, Cambridge, Massachusetts 02139, USA. [2]Beijing National Laboratory for Condensed Matter Physics, and Institute of Physics, Chinese Academy of Sciences, Beijing 100190, China. †These authors contributed equally to this work.
*e-mail: cfang@iphy.ac.cn; liangfu@mit.edu

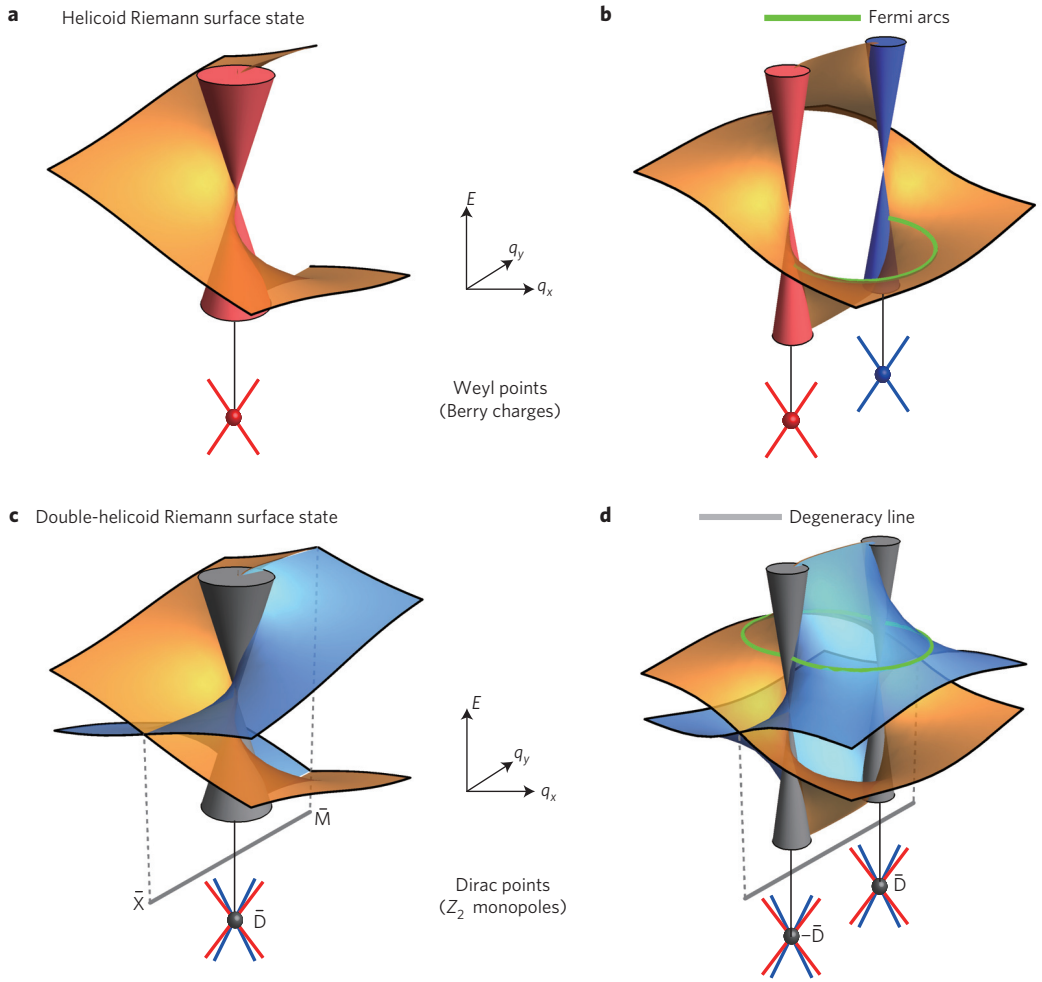


**Figure 1 | The helicoid and double-helicoid surface states. a**, Surface dispersion near the projection of a Weyl point with Chern number +1, where the red solid cones are the projection of the bulk states and the helicoid sheet represents the surface states. This is also the Riemann surface of $\mathrm{Im}[\log(q)]$. **b**, Surface dispersion near the projections of a pair of Weyl points with opposite Chern numbers, where the red and the blue cones represent the bulk states projection, and the green contour is an iso-energy contour also known as a Fermi arc. This is also the Riemann surface of $\mathrm{Im}[\log(q-k_1/q-k_2)]$. **c**, Surface dispersion of the non-symmorphic Dirac semimetal near the Dirac point, where the grey cones represent the projection of bulk states. This is also the Riemann surface of the generating function given in equation (4) in the text. **d**, Surface dispersion near two non-symmorphic Dirac points, with iso-energy contours of two Fermi arcs.

order) zero in complex analysis. Near a simple zero, a general holomorphic function takes the form $f(z)=z-z_0+O[(z-z_0)^2]$ up to an overall factor. As $z$ goes around $z_0$ anticlockwise (clockwise), the phase of $f(z)$ increases (decreases) by $2\pi$. Therefore, the phase of $f(z)$ near $z_0$, or the imaginary part of $\log[f(z)]$, is topologically equivalent to the dispersion of the surface states near the projection of a positive Weyl point. Similarly, one can show that the phase of a holomorphic function near a simple pole is equivalent to the energy dispersion near the projection of a negative Weyl point. This topological equivalence can be expressed as

$$E(\mathbf{q}_\parallel) \sim \mathrm{Im}[\log(q^{\pm 1})] \qquad (1)$$

where $\mathbf{q}_\parallel$ is the surface momentum relative to the Weyl point projection and $q=q_a+iq_b$, and $\pm 1$ corresponds to Weyl point of positive and negative monopole charge. There is one caveat in understanding equation (1): although the generating function on the right-hand side ranges from negative to positive infinity, the energy of the surface bands always merges into the bulk. This infinite winding of the surface dispersion implies that the theory cannot be made ultraviolet-complete in two dimensions, but is consistent only for the surface states of some topologically nontrivial three-dimensional (3D) bulk: a demonstration of the bulk–edge correspondence principle in Weyl semimetals.

In complex analysis, the plot of the real or the imaginary part of a multi-valued holomorphic (meromorphic) function is called a Riemann surface, which is a surface-like configuration that covers the complex plane a finite (compact) or infinite (non-compact) number of times[55]. Equation (1) establishes the topological equivalence between the surface dispersion of a Weyl semimetal and a non-compact Riemann surface. Both share the following characteristic feature: there is no equal-energy (equal height) contour that is both closed and encloses the projection of the Weyl point, a feature that directly leads to the phenomenon of 'Fermi arcs'. This topological equivalence can be extended to the case of multiple Weyl points. If there are projections of two Weyl points at $(k_{1a},k_{1b})$ and $(k_{2a},k_{2b})$, then the corresponding generating function is simply $\log[(q-k_1)(q-k_2)^{-1}]$, where $k_i=k_{ia}+ik_{ib}$, whose imaginary part is plotted in Fig. 1b. Cutting the dispersion at any energy, the iso-energy contour is an arc connecting $\mathbf{k}_1$ and $\mathbf{k}_2$.

## Double-helicoid surface states

A Dirac point can be considered as the superposition of two Weyl points with opposite Chern numbers[16,17], as the 3D massless Dirac

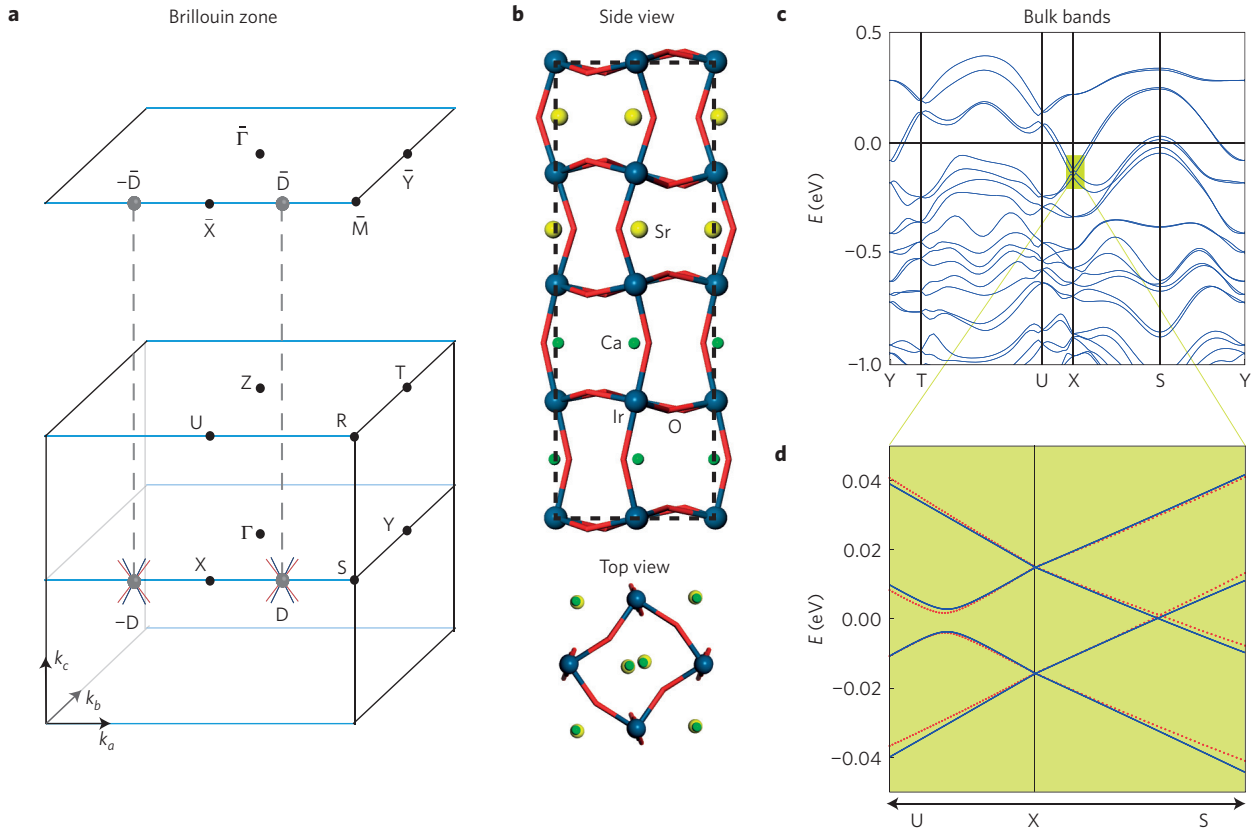


**Figure 2 | Lattice and electronic structure of the iridates superlattice. a**, Brillouin zone and (001)-slab surface Brillouin zone of an orthorhombic lattice with a glide reflection, where the lines of double degeneracy are marked in blue and the Dirac points and their projections are marked by large grey dots. Each Dirac cone can be considered as superimposed positive and negative Weyl cones (red and blue cones centered at the grey dots). **b**, One unit cell of heterostructure superlattice $[(SrIrO_3)_{2m}(CaIrO_3)_{2n}]$ with $m=n=1$. **c**, The bulk band structure of the superlattice along the path YTUXSY, calculated from first principles. **d**, The zoomed-in band structure of the same system near X, where the first-principles results (red dots) are fitted using a tight-binding model modified from the one used in ref. 29 (blue line).

equations decouple into two sets of Weyl equations[56]. The surface state near the projection of a Dirac point is hence a superposition of a helicoid and an anti-helicoid, as shown in Fig. 1c, which cross each other along certain lines, and may have two Fermi arcs[17,18,47]. Yet, if there be no additional symmetry that protects their crossing, hybridization along the crossing lines opens gaps. Then the double-helicoid structure of the surface dispersion is lost and the Fermi arcs also disappear. This has been the case for all Dirac semimetals discovered so far. Below we show that a non-symmorphic symmetry[31,57–65] protects the crossing and with it the double-helicoid surface states.

Consider a three-dimensional system with the following symmetries: a glide reflection, $G$, that reverses the $a$-direction then translates by a half-lattice constant along the $b$-direction, and time-reversal symmetry, $T$. Define the anti-unitary symmetry $\Theta$ as their composition

$$\Theta \equiv G*T : (x,y,z,t) \to (-x, y+1/2, z, -t) \qquad (2)$$

where $(x,y,z)$ are the spatial coordinates along the $a,b,c$-axes in units of the corresponding lattice constants. Equation (2) implies that the momentum of a single quasiparticle, $(k_a,k_b,k_c)$, is sent to $(k_a,-k_b,-k_c)$. Importantly, for the square of $\Theta$ we have

$$\Theta^2 = G^2T^2 = T_{010} = e^{-ik_b} \qquad (3)$$

where $T_{010}$ is the unit lattice translation along the $b$-direction. In particular, at the Brillouin zone boundary $k_b=\pi$, we have $\Theta^2=-1$. This leads to double degeneracy of all states on two high-symmetry lines, UR and XS, analogous to the well-known Kramers' degeneracy[66] (blue lines in the 3D Brillouin zone of Fig. 2a), with the key difference that whereas the latter leads to double degeneracy at high-symmetry points in a spinful system, $\Theta$ leads to double degeneracy along the whole high-symmetry lines in both spinful and spinless systems.

Then we consider the states on the (001)-surface. In the surface Brillouin zone, equation (3) leads to double degeneracy along $\bar{X}\bar{M}$ (blue line in the surface Brillouin zone of Fig. 2a). This degeneracy is exactly what is needed to protect the double-helicoid surface states shown in Fig. 1c: if there be the projection of a Dirac point on $\bar{X}\bar{M}$ and the two helicoids intersect along $\bar{X}\bar{M}$, the symmetry-guaranteed double degeneracy disallows their hybridization. In the double-helicoid dispersion, each iso-energy contour must contain two arcs emanating from the projection of the Dirac point. Owing to time reversal, each projection of the Dirac point at $\bar{D}$ is accompanied by one at $-\bar{D}$. The surface dispersion with two Dirac points is shown in Fig. 1d, and each iso-energy contour contains two arcs connecting $\bar{D}$ and $-\bar{D}$.

As the surface dispersion near a Weyl point projection can be mapped to the Riemann surface of $\log(z)$, a natural question is if the surface dispersion of the Dirac semimetals can also be mapped to some non-compact Riemann surface representing a holomorphic function. The configuration of two surfaces crossing along certain lines reminds us of the Riemann surfaces of holomorphic functions involving a fractional power. For example, $f(z)=\sqrt{z^2}$ has two branches $f_\pm(z)=\pm z$, and the imaginary parts of the two branches

meet each other at the real axis, as $\mathrm{Im}(z)=\mathrm{Im}(-z)=0$ for $z\in\mathbb{R}$. Because the dispersion near the positive and the negative Weyl points are mapped to the phases of $z$ and $z^{-1}$, what we are looking for is a homomorphic function whose two branches are $\log z$ and $\log z^{-1}$. These considerations lead to the following choice

$$E(\mathbf{q}_{\|})\sim\mathrm{Im}[\log(q+q^{-1}+\sqrt{q^2+q^{-2}-2})] \quad (4)$$

where $\mathbf{q}=\mathbf{k}-\bar{\mathrm{D}}$.

According to the bulk–edge correspondence principle, the nontrivial surface state protected by $\Theta$ suggests a nontrivial bulk topology near each Dirac point. In the main text, for concision, we make only the following remarks and leave the detailed discussion of bulk topology to the Methods: a Dirac point is either on XS or UR; on a sphere enclosing the Dirac point, there is a $Z_2$ topological invariant protected by $\Theta$; if inversion is also present and if the system is spinful (with SOC), the invariant can be expressed in terms of rotation eigenvalues of bands along XS or UR, analogous to the Fu–Kane formula for topological insulators[67]. Define $R_2=P*G$, where $P$ is inversion, then $R_2$ is either a two-fold rotation or a two-fold screw rotation, depending on whether the inversion centre is invariant under the glide reflection. In either case, one can prove that, along XS or UR, the two bands that are doubly degenerate owing to $P*T$ have the same eigenvalue of $R_2$, denoted by $\gamma_{2n}(k_a)$, where $2n$ is the band index. Suppose there is a band crossing point at $k_a=k_0$ along XS or US, then its $Z_2$ topological invariant is given by

$$\delta_0=\prod_{n=1,\ldots,N_{\mathrm{occ}}/2}\frac{\gamma_{2n}(k_0+0)}{\gamma_{2n}(k_0-0)} \quad (5)$$

if the inversion centre is invariant under the glide reflection, and by

$$\delta_0=\prod_{n=1,\ldots,N_{\mathrm{occ}}/2}\mathrm{e}^{ik_0}\frac{\gamma_{2n}(k_0+0)}{\gamma_{2n}(k_0-0)} \quad (6)$$

if the inversion centre is variant under the glide reflection, where $N_{\mathrm{occ}}$ is the number of bands below the gap and $k_0\pm 0$ is a number that is close to and larger (smaller) than $k_0$.

In the absence of additional symmetry other than $\Theta$, the Dirac point is not protected and may split into two Weyl points of opposite charge, centred at either XS or UR and related to each other by $\Theta$, termed a 'Weyl dipole'. In this case, we consider a sphere enclosing the Weyl dipole. The Chern number of the sphere is zero owing to the cancellation of monopole charge, but the new $Z_2$ topological charge is nontrivial. In this case, on the surface, Fermi arcs connect Weyl points only from different Weyl dipoles, and the two Weyl points within one Weyl dipole are not connected by a Fermi arc.

Perovskite iridate $SrIrO_3$ was shown to be a topological semimetal with a degenerate nodal line protected by a two-fold screw axis[29,31]. It was found in ref. 29 that under a staggering chemical potential propagating along the [001]-direction, the nodal line is gapped at all but two points. On the basis of this finding, we propose to realize the non-symmorphic Dirac semimetal in a $[(SrIrO_3)_{2m}(CaIrO_3)_{2n}]$ superlattice heterostructure shown in Fig. 2b. For $m=n=1$, we perform a first-principles calculation for the bulk band structure, and find a pair of Dirac points along XS that are close to and symmetric about X, as shown in Fig. 2c. We modify the tight-binding model given in ref. 29 such that its band structure quantitatively matches that from the first-principles calculation near X (Fig. 2d). (Further details of the tight-binding model are given in the Methods.)

On the surface, the double-helicoid requires at least one glide reflection, restricting the surface space group to the following four out of seventeen wallpaper groups: $p1g1$, $p2mg$, $p2gg$ and $p4gm$. We choose the (001)-surface with space group $p1g1$. Using

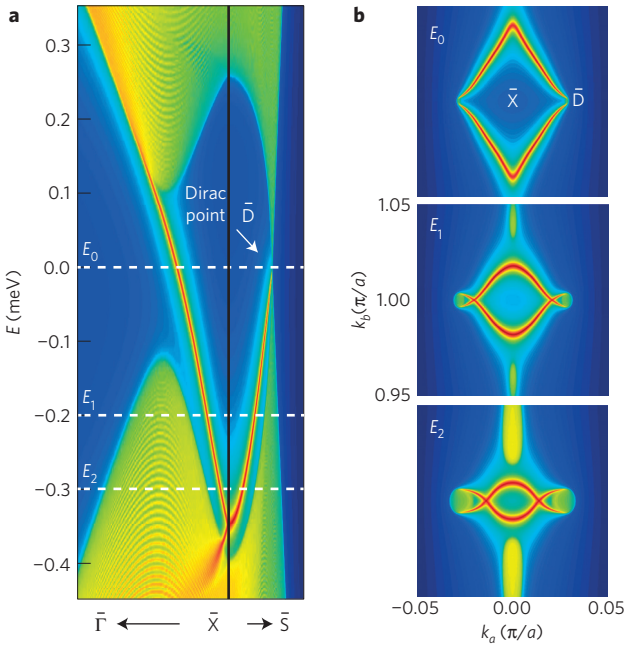


**Figure 3 | Surface state dispersion on the (001)-surface of the iridates superlattice. a**, Spectral weight of the top surface of a (001)-slab, along the path $\bar{\Gamma}$-$\bar{\mathrm{X}}$-$\bar{\mathrm{M}}$, calculated from the tight-binding model used in fitting. **b**, Spectral weight of the (001)-surface at, from top to bottom, $E_{0,1,2}$ respectively.

the fitted tight-binding model, we calculated the spectral weight of the states near the top surface of a (001)-slab, along high-symmetry lines in the surface Brillouin zone (Fig. 3a), and the 2D surface Brillouin zone near $\bar{\mathrm{X}}$ at three different energies (Fig. 3b), where the double Fermi arcs can be seen. We note that as the energy decreases from $E_0$, the energy of the bulk Dirac point, bulk pockets emerge near the projection of the Dirac point and, more importantly, the configuration of the two arcs rotates around the projections of the Dirac points, such that, in Fig. 3b, the two arcs cross each other along $\bar{\mathrm{X}}\bar{\mathrm{M}}$, where the crossing point is protected by $\Theta$.

## Quad-helicoid surface state

Finally, we point out that new types of topological semimetal may exist if additional non-symmorphic symmetries on the surface are present, with their own characteristic surface dispersions. As an example, we assume there be an additional glide plane, $G'$, that is perpendicular to $G$, which strongly restricts the surface space group to the following two: $pmgg$ and $p4gm$. Following similar steps, we find that $\Theta'\equiv G'*T$ guarantees double degeneracy along $\bar{\mathrm{Y}}\bar{\mathrm{M}}$, so that if both $\Theta$ and $\Theta'$ are present, all bands are doubly degenerate along $\bar{\mathrm{X}}\bar{\mathrm{M}}$ and $\bar{\mathrm{Y}}\bar{\mathrm{M}}$. This double degeneracy protects a unique nontrivial surface dispersion consisting of four helicoids near $\bar{\mathrm{M}}$, as shown in Fig. 4, or can be considered as the superposition of the surface dispersions from four Weyl points, of which two are positive and two are negative. This dispersion has a new type of $Z_2$ spectral flow between two perpendicular lines of $\bar{\mathrm{X}}\bar{\mathrm{M}}$ and $\bar{\mathrm{Y}}\bar{\mathrm{M}}$: two bands from a degenerate pair at $\bar{\mathrm{X}}\bar{\mathrm{M}}$ flow to different degenerate pairs at $\bar{\mathrm{Y}}\bar{\mathrm{M}}$. A generic iso-energy contour of this quad-helicoid surface dispersion consists of four Fermi arcs emanating from $\bar{\mathrm{M}}$. Because there is only one $\bar{\mathrm{M}}$ inside the surface Brillouin zone, we argue that no topological charge can be defined for the bulk band crossings which project to $\bar{\mathrm{M}}$, or the Nielson–Ninomiya theorem would be violated. Suppose one uses a 2-manifold, $\partial\mathrm{A}$, to enclose the band crossing point(s) that project to $\bar{\mathrm{M}}$, dividing the Brillouin zone into two parts, A and $\bar{\mathrm{A}}$. If the band crossing points in A

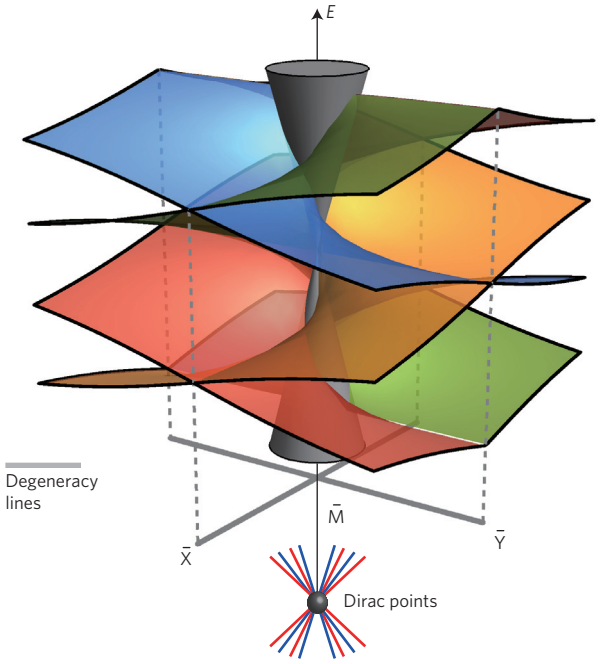


**Figure 4 | Quad-helicoid surface state dispersion.** The surface state consists of two helicoids (blue and red) and two anti-helicoids (green and orange). The blue and the green (also the orange and the red) helicoids cross each other along $\bar{M}\bar{X}$, and the blue and the orange (also the red and the green) helicoids along $\bar{M}\bar{Y}$.

have a topological charge, then on its boundary ∂A a topological invariant can be defined. However, because the Brillouin zone is compact, ∂A is also the boundary of $\bar{A}$, which has presumably no band crossing inside, contradicting the nontrivial invariant on its boundary. We conjecture that the system belongs to the filling-enforced semimetals discussed in refs 57,63, where the band crossings are guaranteed by the space group at certain integer fillings. In this case, the surface dispersion can also be mapped to a non-compact Riemann surface. Because the dispersion can be considered as the superposition of four spiral surfaces, we consider a holomorphic function with four branches. $\Theta$ and $\Theta'$ require that two branches meet along $\bar{X}\bar{M}$ (defined as the real axis) and $\bar{Y}\bar{M}$ (defined as the imaginary axis), respectively. The generating function we choose is

$$E(\mathbf{q}_{\parallel}) \sim \mathrm{Im}[\log(\sqrt{q^2+q^{-2}+2}+\sqrt{q^2+q^{-2}-2})] \qquad (7)$$

where $q=(k_a-\pi)+i(k_b-\pi)$.

## Conclusions

In this paper we theoretically find two new classes of topological semimetals that have multiple Fermi arcs on the surface protected by non-symmorphic glide reflections symmetries and time reversal. We observe that, so far, all topological semimetals with protected Fermi arcs have surface dispersions that are topologically equivalent to helicoid structures that are the non-compact Riemann surfaces representing certain holomorphic functions. Here we remark that although the Riemann surface captures the topology of the surface dispersion near the bulk node projections, it is yet to be shown that, for the surface dispersion defined in the whole surface Brillouin zone, there still exists a corresponding Riemann surface representing an elliptic function. For material realization, we propose superlattice heterostructure $[(SrIrO_3)_{2m}(CaIrO_3)_{2n}]$ as a non-symmorphic Dirac semimetal with two protected Fermi arcs on the (001)-plane.

## Methods

Methods, including statements of data availability and any associated accession codes and references, are available in the online version of this paper.

Received 15 January 2016; accepted 29 April 2016; published online 6 June 2016

## References

1. Murakami, S. Phase transition between the quantum spin Hall and insulator phases in 3D: emergence of a topological gapless phase. *New J. Phys.* **9,** 356 (2007).
2. Chiu, C.-K., Teo, J. C. Y., Schnyder, A. P. & Ryu, S. Classification of topological quantum matter with symmetries. Preprint at http://arXiv.org/abs/1505.03535 (2015).
3. Wan, X., Turner, A. M., Vishwanath, A. & Savrasov, S. Y. Topological semimetal and Fermi-arc surface states in the electronic structure of pyrochlore iridates. *Phys. Rev. B* **83,** 205101 (2011).
4. Hosur, P., Parameswaran, S. A. & Vishwanath, A. Charge transport in Weyl semimetals. *Phys. Rev. Lett.* **108,** 046602 (2012).
5. Son, D. T. & Spivak, B. Z. Chiral anomaly and classical negative magnetoresistance of Weyl metals. *Phys. Rev. B* **88,** 104412 (2013).
6. Liu, C.-X., Ye, P. & Qi, X.-L. Chiral gauge field and axial anomaly in a Weyl semimetal. *Phys. Rev. B* **87,** 235306 (2013).
7. Burkov, A. A., Hook, M. D. & Balents, L. Topological nodal semimetals. *Phys. Rev. B* **84,** 235126 (2011).
8. Burkov, A. A. & Balents, L. Weyl semimetal in a topological insulator multilayer. *Phys. Rev. Lett.* **107,** 127205 (2011).
9. Xu, G., Weng, H., Wang, Z., Dai, X. & Fang., Z. Chern semimetal and the quantized anomalous Hall effect in $HgCr_2Se_4$. *Phys. Rev. Lett.* **107,** 186806 (2011).
10. Fang, C., Gilbert, M. J., Dai, X. & Bernevig, B. A. Multi-Weyl topological semimetals stabilized by point group symmetry. *Phys. Rev. Lett.* **108,** 266802 (2012).
11. Lu, L., Fu, L., Joannopoulos, J. D. & Soljacic, M. Weyl points and line nodes in gyroid photonic crystals. *Nature Photon.* **7,** 294–299 (2013).
12. Liu, J. & Vanderbilt, D. Weyl semimetals from noncentrosymmetric topological insulators. *Phys. Rev. B* **90,** 155316 (2014).
13. Weng, H., Fang, C., Fang, Z., Bernevig, B. A. & Dai, X. Weyl semimetal phase in noncentrosymmetric transition-metal monophosphides. *Phys. Rev. X* **5,** 011029 (2015).
14. Huang, S.-M. *et al*. An inversion breaking Weyl semimetal state in the taas material class. *Nature Commun.* **6,** 7373 (2015).
15. Soluyanov, A. A. *et al*. Type-ii Weyl semimetals. *Nature* **527,** 495–498 (2015).
16. Young, S. M. *et al*. Dirac semimetal in three dimensions. *Phys. Rev. Lett.* **108,** 140405 (2012).
17. Wang, Z. *et al*. Dirac semimetal and topological phase transitions in $A_3Bi$ ($A$ = Na, K, Rb). *Phys. Rev. B* **85,** 195320 (2012).
18. Wang, Z., Weng, H., Wu, Q., Dai, X. & Fang, Z. Three-dimensional Dirac semimetal and quantum transport in $Cd_3As_2$. *Phys. Rev. B* **88,** 125427 (2013).
19. Yang, B.-J. & Nagaosa, N. Classification of stable three-dimensional Dirac semimetals with nontrivial topology. *Nature Commun.* **5,** 4898 (2014).
20. Zeng, M. *et al*. Topological semimetals and topological insulators in rare earth monopnictides. Preprint at http://arXiv.org/abs/1504.03492 (2015).
21. Chiu, C.-K. & Schnyder, A. P. Classification of reflection-symmetry-protected topological semimetals and nodal superconductors. *Phys. Rev. B* **90,** 205136 (2014).
22. Phillips, M. & Aji, V. Tunable line node semimetals. *Phys. Rev. B* **90,** 115111 (2014).
23. Mullen, K., Uchoa, B. & Glatzhofer, D. T. Line of Dirac nodes in hyperhoneycomb lattices. *Phys. Rev. Lett.* **115,** 026403 (2015).
24. Weng, H. *et al*. Topological node-line semimetal in three-dimensional graphene networks. *Phys. Rev. B* **92,** 045108 (2015).
25. Xie, L. S. *et al*. A new form of $Ca_3P_2$ with a ring of Dirac nodes. *APL Mater.* **3,** 083602 (2015).
26. Kim, Y., Wieder, B. J., Kane, C. L. & Rappe, A. M. Dirac line nodes in inversion-symmetric crystals. *Phys. Rev. Lett.* **115,** 036806 (2015).
27. Yu, R., Weng, H., Fang, Z., Dai, X. & Hu, X. Topological node-line semimetal and Dirac semimetal state in antiperovskite $cu_3PdN$. *Phys. Rev. Lett.* **115,** 036807 (2015).
28. Rhim, J.-W. & Kim, Y. B. Landau level quantization and almost flat modes in three-dimensional semimetals with nodal ring spectra. *Phys. Rev. B* **92,** 045126 (2015).
29. Carter, J.-M., Shankar, V. V., Zeb, M. A. & Kee, H.-Y. Semimetal and topological insulator in perovskite iridates. *Phys. Rev. B* **85,** 115105 (2012).

30. Chen, Y., Lu, Y.-M. & Kee, H.-Y. Topological crystalline metal in orthorhombic perovskite iridates. *Nature Commun.* **6,** 6593 (2015).
31. Fang, C., Chen, Y., Kee, H.-Y. & Fu, L. Topological nodal line semimetals with and without spin-orbital coupling. *Phys. Rev. B* **92,** 081201 (2015).
32. Rau, J. G., Lee, E. K.-H. & Kee, H.-Y. Spin-orbit physics giving rise to novel phases in correlated systems: Iridates and related materials. *Annu. Rev. Condens. Matter Phys.* **7,** 57–82 (2016).
33. Lu, L. *et al*. Experimental observation of Weyl points. *Science* **349,** 622–624 (2015).
34. Xu, S.-Y. *et al*. Experimental realization of a topological Weyl semimetal phase with Fermi arc surface states in TaAs. *Science* **349,** 613–617 (2015).
35. Lv, B. Q. Experimental discovery of Weyl semimetal TaAs. *Phys. Rev. X* **5,** 031013 (2015).
36. Shekhar, C. *et al*. Extremely large magnetoresistance and ultrahigh mobility in the topological Weyl semimetal candidate NbP. *Nature Phys.* **11,** 645–649 (2015).
37. Lv, B. Q. *et al*. Observation of Weyl nodes in TaAs. *Nature Phys.* **11,** 724–727 (2015).
38. Yang, L. X. *et al*. Weyl semimetal phase in the non-centrosymmetric compound TaAs. *Nature Phys.* **11,** 728–732 (2015).
39. Xu, S.-Y. *et al*. Discovery of a Weyl fermion state with Fermi arcs in niobium arsenide. *Nature Phys.* **11,** 748–754 (2015).
40. Zhang, C. *et al*. Tantalum monoarsenide: an exotic compensated semimetal. Preprint at http://arXiv.org/abs/1502.00251 (2015).
41. Huang, X. *et al*. Observation of the chiral-anomaly-induced negative magnetoresistance in 3D Weyl semimetal TaAs. *Phys. Rev. X* **5,** 031023 (2015).
42. Liu, Z. K. *et al*. A stable three-dimensional topological Dirac semimetal $Cd_3As_2$. *Nature Mater.* **13,** 677–681 (2014).
43. Liu, Z. K. Discovery of a three-dimensional topological Dirac semimetal, $Na_3Bi$. *Science* **343,** 864–867 (2014).
44. Neupane, M. *et al*. Observation of a three-dimensional topological Dirac semimetal phase in high-mobility $Cd_3As_2$. *Nature Commun.* **5,** 3786 (2014).
45. He, L. P. *et al*. Quantum transport evidence for the three-dimensional Dirac semimetal phase in $Cd_3As_2$. *Phys. Rev. Lett.* **113,** 246402 (2014).
46. Jeon, S. *et al*. Landau quantization and quasiparticle interference in the three-dimensional Dirac semimetal $Cd_3As_2$. *Nature Mater.* **13,** 851–856 (2014).
47. Xu, S.-Y. *et al*. Observation of Fermi arc surface states in a topological metal. *Science* **347,** 294–298 (2015).
48. Xiong, J. *et al*. Evidence for the chiral anomaly in the Dirac semimetal $Na_3Bi$. *Science* **350,** 413–416 (2015).
49. Bian, G. *et al*. Topological nodal-line fermions in the spin–orbit metal $PbTaSe_2$. *Nature Commun.* **7,** 10556 (2016).
50. Potter, A. C., Kimchi, I. & Vishwanath, A. Quantum oscillations from surface Fermi arcs in Weyl and Dirac semimetals. *Nature Commun.* **5,** 5161 (2014).
51. Kargarian, M., Randeria, M. & Lu, Y.-M. Are the double Fermi arcs of Dirac semimetals topologically protected? Preprint at http://arXiv.org/abs/1509.02180v1 (2015).
52. Matsuno, J. *et al*. Engineering a spin-orbital magnetic insulator by tailoring superlattices. *Phys. Rev. Lett.* **114,** 247209 (2015).
53. Weyl, H. *The Concept of a Riemann Surface* (Dover, 2009).
54. Li, S. & Andreev, A. V. Spiraling Fermi arcs in Weyl materials. *Phys. Rev. B* **92,** 201107 (2015).
55. Knopp, K. *Theory of Functions Parts I and II, Two Volumes Bound as One, Part II* (Dover, 1996).
56. Peskin, M. E. *An Introduction to Quantum Field Theory* (Westview, 1995).
57. Parameswaran, S. A., Turner, A. M., Arovas, D. P. & Vishwanath, A. Topological order and absence of band insulators at integer filling in non-symmorphic crystals. *Nature Phys.* **9,** 299–303 (2013).
58. Freed, D. S. & Moore, G. W. Twisted equivariant matter. *Ann. Henri Poincare* **14,** 1927–2023 (2013).
59. Liu, C.-X., Zhang, R.-X. & VanLeeuwen, B. K. Topological nonsymmorphic crystalline insulators. *Phys. Rev. B* **90,** 085304 (2014).
60. Fang, C. & Fu, L. New classes of three-dimensional topological crystalline insulators: Nonsymmorphic and magnetic. *Phys. Rev. B* **91,** 161105 (2015).
61. Shiozaki, K., Sato, M. & Gomi, K. $Z_2$ topology in nonsymmorphic crystalline insulators: Möbius twist in surface states. *Phys. Rev. B* **91,** 155120 (2015).
62. Varjas, D., de Juan, F. & Lu, Y.-M. Bulk invariants and topological response in insulators and superconductors with nonsymmorphic symmetries. *Phys. Rev. B* **92,** 195116 (2015).
63. Watanabe, H., Po, H. C., Vishwanath, A. & Zaletel, M. P. Filling constraints for spin-orbit coupled insulators in symmorphic and non-symmorphic crystals. *Proc. Natl Acad. Sci. USA* **112,** 14551–14556 (2015).
64. Lu, L. *et al*. Symmetry-protected topological photonic crystal in three dimensions. *Nature Phys.* **12,** 337–340 (2016).
65. Wang, Z., Alexandradinata, A., Cava, R. J. & Bernevig, B. A. Hourglass fermions. *Nature* **532,** 189–194 (2016).
66. Kramers, H. Théorie générale de la rotation paramagnétique dans les cristaux. *Proc. Amsterdam Akad.* **33,** 959–972 (1930).
67. Fu, L. & Kane, C. Topological insulators with inversion symmetry. *Phys. Rev. B* **76,** 045302 (2007).


## Acknowledgements

We thank T. H. Hsieh for discussions. C.F. thanks Y. Chen for helpful discussions on the tight-binding model. C.F. thanks J.L. for fruitful discussions on potential material systems. C.F. and L.F. were supported by S3TEC Solid State Solar Thermal Energy Conversion Center, an Energy Frontier Research Center funded by the US Department of Energy (DOE), Office of Science, Basic Energy Sciences (BES), under Award no. DE-SC0001299/DE-FG02-09ER46577. C.F. was also supported by the National Thousand-Young-Talents Program of China. L.L. was supported in part by USARO through the ISN under Contract no. W911NF-13-D-0001, in part by the MRSEC Program of the NSF under Award no. DMR-1419807, and in part by the MIT S3TEC EFRC of DOE under Grant no. DE-SC0001299. J.L. was supported by the STC Center for Integrated Quantum Materials, NSF Grant no. DMR-1231319.

## Author contributions

C.F. and L.L. conceived the mapping between surface state dispersions and helicoids; L.F. planned the project; C.F. and L.F. performed the band topology analysis; J.L. performed the first-principles calculation and all authors contributed to the preparation of the manuscript.

## Additional information

Reprints and permissions information is available online at www.nature.com/reprints. Correspondence and requests for materials should be addressed to C.F. or L.F.

## Competing financial interests

The authors declare no competing financial interests.

## Methods

**$Z_2$ invariant protected by $G*T$.** The bulk invariant is defined on a sphere in the Brillouin zone that encloses some band crossings (either nodal points or nodal lines), and on the surface of that sphere, the conduction and the valence bands have a finite direct gap and hence can be separated. For our case, owing to $\Theta$, the generic band crossing is a pair of opposite Weyl points symmetric about either XS or UR. We use a sphere centred at $\mathbf{k}_0$, a point on XS, with radius $k_r$. Each point on the sphere is parameterized by $(\theta,\phi)$:

$$(k_a,k_b,k_c)=(k_{0a}+k_r\cos\theta,k_{0b}+k_r\sin\theta\cos\phi,k_{0c}+k_r\sin\theta\sin\phi) \tag{8}$$

The derivation of the $Z_2$ invariant on a sphere invariant under $\Theta=G*T$ closely follows the derivation of the $Z_2$ invariant of 2D topological insulators. (See ref. 67.)

First we parameterize the sphere such that, under $\Theta$, a point at $(\theta,\phi)$ is mapped to $(\theta,\phi+\pi)$. Because the total Chern number on the sphere vanishes, we can hence in principle choose a smooth gauge for all occupied bands, denoted by $|u_{n\in\mathrm{occ}}(\theta,\phi)\rangle$. We can then define the following sewing matrix

$$W_{mn}(\theta,\phi)=\langle u_m(\theta,\phi+\pi)|\Theta|u_n(\theta,\phi)\rangle \tag{9}$$

At $\theta=0,\pi$, we have

$$\begin{aligned}W_{mn}(0/\pi)&=\langle u_m(0/\pi)|\Theta|u_n(0/\pi)\rangle\\&=(\langle\Theta u_m(0/\pi)|\Theta^2|u_n(0/\pi)\rangle)^2\\&=-\langle u_n(0/\pi)|\Theta|u_m(0/\pi)\rangle\\&=-W_{nm}(0/\pi)\end{aligned} \tag{10}$$

that is,

$$W=-W^T(0/\pi) \tag{11}$$

Therefore, we can define the following $Z_2$ quantity

$$\delta_0=\frac{\mathrm{Pf}[W(0)]}{\sqrt{\det[W(0)]}}\frac{\mathrm{Pf}[W(\pi)]}{\sqrt{\det[W(\pi)]}} \tag{12}$$

where Pf stands for the Pfaffian of an antisymmetric matrix. Equation (12) defines a $Z_2$ quantity which is either $+1$ or $-1$, because $\mathrm{Pf}^2=\det$ in general.

To prove that the $Z_2$ quantity is also gauge invariant, consider changing the gauge by a smooth unitary $N_{\mathrm{occ}}$-by-$N_{\mathrm{occ}}$ matrix $U(\theta,\phi)$

$$|u'_m(\theta,\phi)\rangle=\sum_n U_{mn}(\theta,\phi)|u_n(\theta,\phi)\rangle \tag{13}$$

It is straightforward to see that, after the transform, the sewing matrix becomes

$$W'(\theta,\phi)=U^T(\theta,\phi+\pi)W(\theta,\phi)U(\theta,\phi) \tag{14}$$

so that at $\theta=0,\pi$

$$\mathrm{Pf}[W'(0/\pi)]=\det[U(0/\pi)]\mathrm{Pf}[W(0/\pi)] \tag{15}$$

$$\begin{aligned}\det[W'(0/\pi)]&=\det[U^T(0/\pi)]\det[W(0/\pi)]\det[U(0/\pi)]\\&=\det[W(0/\pi)]\det^2[U(0/\pi)]\end{aligned}$$

Substituting equations (15) into equation (12), we find

$$\delta'_0=\delta_0 \tag{16}$$

**Simplification of the $Z_2$ invariant.** In this section, we show how the $Z_2$ invariant given in terms of Pfaffians in equation (12) simplifies in the presence of inversion symmetry in a spinful system. We will closely follow the derivation of the original Fu–Kane formula in topological insulators with inversion symmetry, which can be briefly summarized as follows: the bands at time-reversal invariant momenta are also eigenstates of the inversion; each state and its time-reversal partner have the same inversion eigenvalue, so that each Kramers' pair at a time-reversal invariant momentum maps to an eigenvalue of either $+1$ or $-1$; the product of the inversion eigenvalues of all occupied Kramers' pairs at all time-reversal invariant momenta is the same as the Pfaffian invariant.

In our case, the time-reversal symmetry is replaced by $\Theta=G*T$, and the points that are invariant under $\Theta$ are $\theta=0,\pi$ on the sphere. The inversion symmetry itself is not a good quantum number at these points, but the composition symmetry $R_2\equiv P*G$ is. We will now prove that each degenerate pair of states at $\theta=0,\pi$ has the same eigenvalue of $R_2$.

We distinguish two cases: the inversion centre within the glide plane and the inversion centre not within the glide plane. A generic inversion operation takes the form

$$P:(x,y,z)\to\left(\frac{\lambda}{2}-x,\frac{\mu}{2}-y,\frac{\nu}{2}-z\right) \tag{17}$$

where $\lambda,\mu,\nu=0,1$. If $\lambda=0$, then the inversion centre $(0,\mu,\nu)/2$ is on the glide plane; if $\lambda=1$, then the inversion centre $(1/2,\mu/2,\nu/2)$ is away from the glide plane.

If the inversion centre is inside the glide plane, then we have

$$R_2:(x,y,z)\to\left(x,\frac{\mu}{2}-y-\frac{1}{2},\frac{\nu}{2}-z\right) \tag{18}$$

and

$$R_2^2:(x,y,z)\to(x,y,z) \tag{19}$$

However, because in spin space $R^2$ is equivalent to a full spin rotation, we have

$$R^2=-1 \tag{20}$$

Also, the commutation relation between $R_2$ and $\Theta$ can be shown to be

$$R_2\Theta=T_{010}\Theta R_2=\mathrm{e}^{-ik_b}\Theta R_2 \tag{21}$$

From equation (20), each state at $\theta=0,\pi$ is also an eigenstate of $R_2$ with eigenvalue of either $+i$ or $-i$. Using equation (21), we see that for each eigenstate of $R_2$ with eigenvalue $+i$

$$R_2\Theta|+i\rangle=\mathrm{e}^{-ik_b}\Theta R_2|+i\rangle=-\mathrm{e}^{-ik_b}i\Theta|+i\rangle \tag{22}$$

that is, $\Theta|+i\rangle$ is an eigenstate of $R_2$ with eigenvalue $-\mathrm{e}^{-ik_b}i=+i$ at $\theta=0,\pi$. Hence the two states in one degenerate pair at $\theta=0,\pi$ have the same eigenvalue of $R_2$, because $k_b=\pi$. Following ref. 67, we see that the $Z_2$ invariant can be expressed in terms of these eigenvalues

$$\delta_0=\prod_{n=1,\ldots,N_{\mathrm{occ}}/2}\frac{\gamma_{2n}(0)}{\gamma_{2n}(\pi)} \tag{23}$$

If the inversion centre is away from the glide plane, we have

$$R_2:(x,y,z)\to\left(x+\frac{1}{2},\frac{\mu}{2}-y-\frac{1}{2},\frac{\nu}{2}-z\right) \tag{24}$$

which is in fact a two-fold screw axis. The square of $R_2$ is

$$R_2^2:(x,y,z)\to(x+1,y,z) \tag{25}$$

Again, considering the spin rotation in $R_2$, we find that the eigenvalues are $\pm ie^{-ik_a/2}$ from equation (25). The commutation relation between $R_2$ and $\Theta$ is

$$R_2\Theta=T_{110}\Theta R_2=\mathrm{e}^{-ik_a-ik_b}\Theta R_2 \tag{26}$$

so that, for an eigenstate of $R_2$ with eigenvalue $+ie^{-ik_a/2}$, we have

$$R_2\Theta|+ie^{-ik_a/2}\rangle=-ie^{-ik_a/2-ik_b}|+ie^{-ik_a/2}\rangle \tag{27}$$

Equation (27) shows that at $\theta=0,\pi$ (where $k_b=\pi$), the two degenerate states have the same eigenvalue of $R_2$. Following ref. 67, we secure the following expression for the Pfaffian invariant

$$\delta_0=\prod_{n=1,\ldots,N_{\mathrm{occ}}/2}\mathrm{e}^{ik_0}\frac{\gamma_{2n}(0)}{\gamma_{2n}(\pi)} \tag{28}$$

**Splitting of the non-symmorphic Dirac point in the absence of inversion.** In this section, we lift the symmetry of inversion, keeping glide reflection and time reversal. Without the inversion, the bands are in general nondegenerate, and a single Dirac point splits into two Weyl points. Because glide reflection inverts the monopole charge of a Weyl point and time reversal preserves it, the configuration of the split Dirac point is such that $W_1$ is related to $W_2$ by $\Theta=G*T$, whereas $W'_{1,2}$

are related to $W_{1,2}$ by time reversal, in the presence of an inversion-breaking perturbation. Yet it is important to note that, even in this case, the system is not a generic Weyl semimetal, because each pair of Weyl points related by $G*T$, $W_1$ and $W_2$, for example, carries a $Z_2$ topological charge. Consider a sphere enclosing such a pair, and the definition of the $Z_2$ invariant depends only on the presence of $G*T$. Therefore, if this invariant is nontrivial in the presence of inversion due to the Dirac point, it remains nontrivial after the splitting. This $Z_2$ topological charge has two consequences: on the surface preserving $G$, the Fermi arcs must not connect the projections of Weyl points that are related by $G*T$; and there must be an even number of such pairs of Weyl points as a consequence of the Nielson–Ninomiya theorem.

**Some details of the numerics.** The band structures of $(SrIrO_3)_{2m}(CaIrO_3)_{2n}$ are calculated in the framework of density functional theory (DFT) including the Hubbard $U$, as implemented in the Vienna *ab initio* simulation package (VASP)[68] using the generalized gradient approximation (GGA) of the exchange-correlation function in the Perdew–Burke–Ernzerhof (PBE) form[69]. The projector augmented wave method[70] was applied to model the core electrons. Monkhorst–Pack **k**-point sampling of $4\times4\times2$ was used for $(m=1,n=1)$. Energy cutoff of the plane wave basis was fully tested, and atomic structures were optimized with maximal residual forces smaller than 0.01 eV Å$^{-1}$. Spin–orbit coupling (SOC) was included in all calculations. For the Hubbard $U<2$, all the results are similar, so here we show only the results for $U=0$ for the sake of simplicity.

For $SrIrO_3$ (that is, $m=1,n=0$), we obtain results similar to those in a previous study[29], with the Dirac nodal line around the Fermi energy. For $(SrIrO_3)_2(CaIrO_3)_2$, the Dirac nodal line folds around X point owing to an enlarged unit cell. One then expects the line to be gapped at most points as a result of the broken two-fold screw rotation, leaving a pair of Dirac points along XS protected by $G$. These properties have been confirmed by the first-principles calculation.

To study the surface states of $(SrIrO_3)_2(CaIrO_3)_2$, we employ a tight-binding model obtained by adding several mass terms to the model given in ref. 29:

$$H=\begin{pmatrix} H_0+H_1 & T+T_1 & 0 & \mathrm{e}^{-ik_z}(T-T_1)^\dagger \\ (T+T_1)^\dagger & (H_0-H_1)\epsilon+m_1 & T-T_1 & 0 \\ 0 & (T-T_1)^\dagger & H_0+H_1 & T+T_1 \\ \mathrm{e}^{ik_z}(T-T_1) & 0 & (T+T_1)^\dagger & H_0-H_1 \end{pmatrix}$$

where $H_0=2t_\mathrm{p}(\cos k_x+\cos k_y)\tau_x$,
$H_1=(t_{1\mathrm{p}}\cos k_y+t_{2\mathrm{p}}\cos k_x)s_y\tau_y-(t_{1\mathrm{p}}\cos k_x+t_{2\mathrm{p}}\cos k_y)s_x\tau_y$,
$T=t_\mathrm{p}-it_\mathrm{d}(\sin k_x s_y+\sin k_y s_x)\tau_y$, $T_1=m_2(\sin k_x s_x+\sin k_y s_y)\tau_x$. By fitting with the DFT results, we can get the corresponding parameters, $t_\mathrm{p}=-0.0785, t_\mathrm{d}=0.053, t_{1\mathrm{p}}=-0.1331, t_{2\mathrm{p}}=0.1597, m_1=0.0112, m_2=0.0006, \epsilon=0.3078$ in units of eV. The surface band structures are calculated in a semi-infinite geometry by means of the recursive Green's function method[71].

**Data availability.** The data that support the plots within this paper and other findings of this study are available from the corresponding author on request.

## References


68. Kress, G. & Furthmuller, J. Efficient iterative schemes for *ab initio* total-energy calculations using a plane-wave basis set. *Phys. Rev. B* **54,** 11169 (1996).
69. Perdew, J. P., Burke, K. & Ernzerhof, M. Generalized gradient approximation made simple. *Phys. Rev. Lett.* **77,** 3865–3868 (1996).
70. Blochl, P. E. Projector augmented-wave method. *Phys. Rev. B* **50,** 17953 (1994).
71. Sancho, M. P. L., Sancho, J. M. L. & Rubio, J. Highly convergent schemes for the calculation of bulk and surface Green functions. *J. Phys. F: Met. Phys.* **15,** 851–858 (1985).